

Polymer dynamics in semidilute solution during electrospinning: A simple model and experimental observations

Israel Greenfeld,¹ Arkadii Arinstein,¹ Kamel Fezzaa,² Miriam H. Rafailovich,³ and Eyal Zussman¹

¹*Department of Mechanical Engineering, Technion, Israel Institute of Technology, Haifa 32000, Israel*

²*Advanced Photon Source, Argonne National Laboratory, Argonne, Illinois 60439, USA*

³*Department of Materials Science and Engineering, State University of New York, Stony Brook, New York 11794-2275, USA*

(Received 25 July 2011; published 14 October 2011)

Electrospun polymer nanofibers demonstrate outstanding mechanical and thermodynamic properties as compared to macroscopic-scale structures. Our previous work has demonstrated that these features are attributed to nanofiber microstructure [Nat. Nanotechnol. **2**, 59 (2007)]. It is clear that this microstructure is formed during the electrospinning process, characterized by a high stretching rate and rapid evaporation. Thus, when studying microstructure formation, its fast evolution must be taken into account. This study focuses on the dynamics of a highly entangled semidilute polymer solution under extreme longitudinal acceleration. The theoretical modeling predicts substantial longitudinal stretching and transversal contraction of the polymer network caused by the jet hydrodynamic forces, transforming the network to an almost fully stretched state. This prediction was verified by x-ray phase-contrast imaging of electrospinning jets of poly(ethylene oxide) and poly(methyl methacrylate) semidilute solutions, which revealed a noticeable increase in polymer concentration at the jet center, within less than 1 mm from the jet start. Thus, the proposed mechanism is applicable to the initial stage of the microstructure formation.

DOI: [10.1103/PhysRevE.84.041806](https://doi.org/10.1103/PhysRevE.84.041806)

PACS number(s): 83.80.Rs, 47.85.md, 83.50.Jf, 47.61.-k

I. INTRODUCTION

The size-dependent behavior of nano-objects is a generally accepted phenomenon, observed in polymer nanofibers [1,2], metallic nanowires [3], and thin polymer films [4]. Experimental studies have demonstrated the effect of size on the mechanical, thermomechanical, and thermodynamic properties of nano-objects. For example, the elastic modulus of nanowires [3], polypyrrole nanotubes [5], and electrospun polystyrene and nylon-66 nanofibers [1,2] sharply increases when their diameter becomes sufficiently small. Also, a shift in the glass transition and melting temperatures is observed in polymer nano-objects [6]. All proposed mechanisms attributing this behavior to surface tension [5] or near-surface layers [7,8] do not satisfactorily explain the above phenomena. Moreover, our recent work has demonstrated that the contribution of surface energy to size-dependent elasticity of nano-objects is negligible [9]. Overall, the physical mechanisms governing the size-dependent behavior of nano-objects are largely unclear.

Further progress in understanding of the features of electrospun polymer nanofibers influencing their behavior requires examination of their internal structure, more specifically, the supermolecular structures in the amorphous regions of the polymer matrix, as well as crystallite ordering. At the initial stages of such analyses, the impact of fabrication conditions upon the final state of the polymer matrix of as-spun nanofibers must be determined. In doing so, the high strain rate (on the order 10^3 s^{-1}) acting during electrospinning [10–16], must be considered. This dominant factor is believed to cause stretching and orientation of polymer chains, as indicated by in-process measurements of jets, using birefringence [17] and Raman [18] techniques.

In parallel, extremely rapid evaporation of solvents adversely affects the polymer matrix macrostructure of as-spun nanofibers. Rapid evaporation first leads to formation of a

solid skin, followed by further evaporation from the liquid core, leaving voids previously occupied by solvents and allowing partial relaxation of the matrix. This frequently induces generation of a heterogeneous and porous fiber structure [19,20]. Theoretical analyses [21,22], confirmed by experimental observations [19] and computerized simulations [23], demonstrated that a sharp increase in polymer density at the fiber-vapor interface is induced upon rapid solvent evaporation, consequently increasing heterogeneity and porosity. Thus, heterogeneous, high-porosity fiber structures can be formed under certain electrospinning conditions [see Fig. 1(a)].

At the same time, skin formation prevents further stretching and orientation of polymer chains within the semiliquid fiber core. Relaxation of the nonequilibrium state of the stretched macromolecules consequentially occurs, with no detectable influence of the fabrication conditions on the final state of the polymer matrix of as-spun nanofibers. On the other hand, spinning conditions resulting in homogeneous as-spun fiber structures can be selected [see Fig. 1(b)]. In such cases, relaxation of stretched polymer chains is suppressed, and the effect of fabrication conditions on the final state of the nanofiber polymer matrix should be noticeable.

While the physical mechanism underlying formation of the porous structure of as-spun nanofibers is well understood [19,21,22], the physical principles governing generation of the homogeneous fiber structure demand clarification. Significant insight is expected to emerge from examination of the evolution of the polymer system within the semidilute solution jet during electrospinning. The mechanism required to form an homogeneous fiber structure can be proposed based on the assumption that the polymer system, which is an interconnected network of subchains, undergoes substantial stretching during electrospinning.

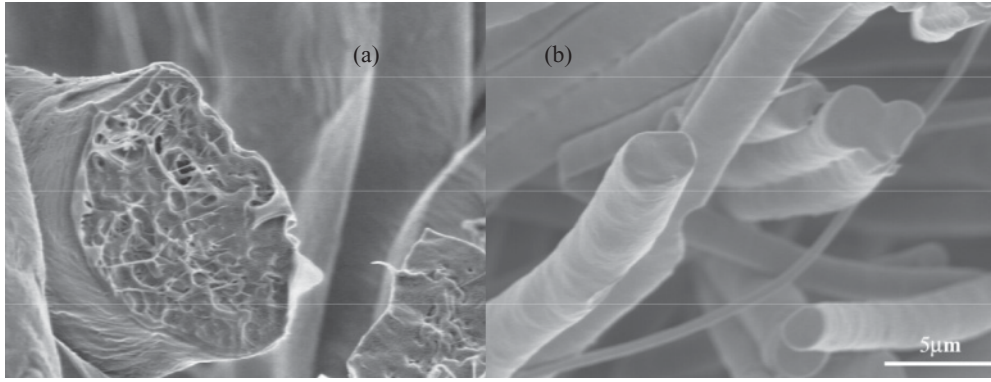


FIG. 1. SEM images of electrospun nanofibers fabricated from 10 wt% PCL (Mw 80 kDa) in DCM/DMF (75:25 wt%), in an electric field of 0.63 kV/cm [24]. (a) Heterogeneous fibers fabricated at a flow rate of 20 ml/h and (b) homogeneous fibers fabricated at a flow rate of 3 ml/h.

In order to confirm the stretching hypothesis, a theoretical model describing the polymer system as an entangled network and its evolution in the initial stage of electrospinning is presented. The conformational state of individual subchains is clarified by a three-dimensional (3D) random-walk simulation. The theoretical analysis and simulations show that the initial equilibrium state of the polymer network transforms to an almost fully stretched state along the jet. This stretching is accompanied by network contraction across the jet. These theoretical results were experimentally confirmed by x-ray phase-contrast imaging of electrospinning jets of PEO (polyethylene oxide) and PMMA (polymethyl methacrylate) semidilute solutions, which revealed a noticeable polymer concentration increase at the jet center, within less than 1 mm from the jet start.

II. THEORETICAL MODELING

A. Velocity and radius of an electrospinning jet

Under an electric field, the moving solution jet accelerates, so that its local velocity contains both longitudinal and radial components. Hydrodynamic analysis demonstrates that in the jet beginning the longitudinal velocity can be approximated by a parabolic profile, whereas the radial velocity component increases linearly along the jet [25]:

$$v_z \approx v_0 \left(1 + \frac{z}{z_0}\right)^2, \quad v_r = -\frac{r}{2} \frac{\partial v_z}{\partial z} \approx -v_0 \left(1 + \frac{z}{z_0}\right) \frac{r}{z_0}, \quad (1)$$

and, therefore, the jet has the hyperpolic form:

$$r_J(z) = \frac{r_0}{1 + z/z_0}, \quad (2)$$

where v_0 is the jet initial velocity and r_0 is the jet initial radius. The characteristic length z_0 determines the scale of velocity increase and depends on the solution's flow rate, viscosity, electric field, and electric conductivity. Typical values of these parameters, measured by optical microscopy of the jet [15,16], and substantiated by our experimental observations are $v_0 \sim (1-5) \times 10^{-2}$ m/s and $z_0 \sim (0.5-1) \times 10^{-3}$ m. Such hydrodynamic flux with increasing longitudinal velocity influences on the polymer macromolecules results in

their nonequilibrium conformation state and heterogeneous distribution inside the jet.

The velocity increase of the liquid jet is clearly limited, due to viscosity increase as a result of solvent evaporation and final solidification of the jet. Since this work focuses only on the initial stage of jet spinning, the above saturation effect lies beyond the scope of this paper.

B. Polymer system structure

It is well known that viscoelasticity is a prerequisite for polymer solution spinnability, meaning that spinnable solutions are semidilute, highly entangled. Therefore, the polymer system is assumed to be a network, whose connectivity is provided by topological knots [11] [see Fig. 2(a)]. The sections of macromolecules between two adjacent topological knots are called subchains, which feature a conformation at equilibrium that corresponds to their nonzero end-to-end distance, even in the absence of external force. This end-to-end distance is equal to the distance between two topological knots or to an average

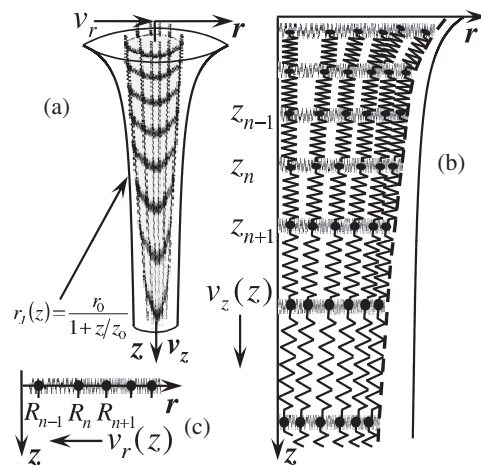


FIG. 2. (a) Illustration of polymer network stretching in an electrospinning jet. (b) Definition of an effective 1D system describing polymer network stretching in the axial direction. (c) Definition of an effective 1D system describing polymer network contraction in the radial direction.

mesh size ξ_0 of the network in a semidilute solution

$$\xi_0 \propto R_g(c/c^*)^{\nu/(1-3\nu)}, \quad (3)$$

where $R_g \propto aN^\nu$ is the end-to-end distance of a polymer coil, c is the mass concentration of the polymer solution, c^* is the crossover concentration of macromolecules overlap, N is the number of monomers in a polymer chain, and a is the monomer scale. Solvents usually used in such systems vary between good and moderately poor solvents; so the conformation of a polymer chain should be a Gaussian or swelled coil ($1/2 < \nu < 3/5$). On the other hand, the polymer concentration in spinnable solutions is relatively high $[(5-10) \times c^*]$, and this prevents a coil swelling. Therefore, for simplicity, we can assume that $\nu = 1/2$. Assuming Gaussian statistics of subchains, one can estimate the number of monomers in a subchain as follows:

$$N_s = (\xi_0/a)^2 = N(c/c^*)^{-2}. \quad (4)$$

Thus, the elements of the system which undergo noticeable stretching are the above-defined subchains. The evolution of subchain conformation under stretching of the polymer network will now be examined.

C. Axial stretching of an entangled polymer network during electrospinning

The polymer network in question can be approximated by a lattice model of "beads" and linear "springs," similar to the Rouse model. Each bead represents a topological knot and is connected to six adjacent beads by springs, or polymer subchains, demonstrating Gaussian statistics, leading to a linear force-elongation relationship. The averaging of the system over the jet cross section results in a one-dimensional chain of springs that interconnects the beads, each having an effective subchain mass, m . The beads are influenced by an effective hydrodynamic force proportional to the effective subchain size, $a_{\text{eff}} \propto \xi_0$, as well as entropic elastic forces from its two neighbors [see Fig. 2(b)]. The dynamics of this chain of springs can be described by the following difference-differential equation:

$$m \frac{d^2 z_n}{dt^2} = a_{\text{eff}} \eta \left[v_z(z_n) - \frac{dz_n}{dt} \right] + \frac{T}{\xi_0^2} \{ [z_{n+1} - z_n - \xi_0] - [z_n - z_{n-1} - \xi_0] \}, \quad (5)$$

where η is the effective viscosity of the dilute solution surrounding the polymer network, v_z is the jet axial velocity from Eq. (1), and T/ξ_0^2 is the entropic elasticity of polymer subchains, where T is the temperature in units of the Boltzmann constant k_B .

The difference equation (5) can be approximated by the following differential equation:

$$\frac{d^2 z(l,t)}{dt^2} = \frac{a_{\text{eff}} \eta}{m} \left[v_z(z) - \frac{dz(l,t)}{dt} \right] + c_{\text{net}}^2 \frac{d^2 z(l,t)}{dl^2}, \quad (6)$$

where $c_{\text{net}} = \sqrt{T/m} \sim 0.3$ m/s is the "sound" velocity in the polymer network and $l = \xi_0 n$. As the polymer network demonstrates only entropic elasticity of a semidilute solution, it is much lower than the sound velocity in solid polymer systems. The polymer is at equilibrium at the cross section

$z = -z_0$, while free boundary conditions are assumed at $z = +\infty$.

The partial differential equation (6) allows one to find a self-similar solution. Indeed, upon introduction of the dimensionless, self-simulated variable $\zeta = (l + v_0 t)/z_0$ and the function $\hat{z}(\zeta) = z(l,t)/z_0$, Eq. (6) can be rewritten as an ordinary differential equation:

$$\frac{d^2 \hat{z}(\zeta)}{d\zeta^2} = -\alpha \left[\hat{v}_z(\hat{z}) - \frac{d\hat{z}(\zeta)}{d\zeta} \right]; \quad (7)$$

here $\alpha = z_0 v_0 a_{\text{eff}} \eta / [m(c_{\text{net}}^2 - v_0^2)] \sim 10^3 - 10^4 \gg 1$ is a dimensionless parameter and $\hat{v}_z(\hat{z}) = v_z(z)/v_0$.

Using the substitution $d\hat{z}(\zeta)/d\zeta = P(\hat{z})$, the second-order differential equation (7) can be reduced to a first-order equation:

$$\frac{dP(\hat{z})}{d\hat{z}} = -\alpha \left[\frac{\hat{v}_z(\hat{z})}{P(\hat{z})} - 1 \right]. \quad (8)$$

The solution of Eq. (8) can be obtained, using a $(1/\alpha)$ approximation. Assuming that

$$\frac{\hat{v}_z(\hat{z})}{P(\hat{z})} - 1 = \frac{1}{\alpha} P_1(\hat{z}) + \dots, \quad (9)$$

we obtain $P_1(\hat{z}) = -d\hat{v}_z(\hat{z})/d\hat{z}$, so within accuracy of $(1/\alpha)^2$ the function $P(\hat{z})$ is

$$P(\hat{z}) = \frac{d\hat{z}(\zeta)}{d\zeta} = \frac{dz(l,t)}{dl} \approx \frac{\hat{v}_z(\hat{z})}{1 - \frac{1}{\alpha} d\hat{v}_z(\hat{z})/d\hat{z}}, \quad (10)$$

and the function $\hat{z}(\zeta)$ can be obtained as an inverse function:

$$\zeta(\hat{z}) = \int_0^{\hat{z}} \frac{dx}{\hat{v}_z(x)} - \frac{1}{\alpha} \ln[\hat{v}_z(\hat{z})]. \quad (11)$$

The stretching of the polymer network is characterized by Eq. (10), which allows one to determine the stretched mesh size ξ_{\parallel} along the jet

$$\xi_{\parallel} = \xi_0 \frac{dz(l,t)}{dl} \approx \frac{\xi_0 \hat{v}_z(\hat{z})}{1 - \frac{1}{\alpha} d\hat{v}_z(\hat{z})/d\hat{z}}. \quad (12)$$

The obtained dependence ξ_{\parallel}/aN_s is shown in Fig. 3 with respect to the position z along the jet, for longitudinal velocity v_z from Eq. (1). Note that the stretching of the polymer subchains exceeds the maximal possible elongation corresponding to fully stretched subchains.

The region where the stretched subchains are approaching full extension, i.e., $\xi_{\parallel} \simeq aN_s$, can be estimated using Eq. (12) for $\alpha \gg 1$ resulting in $\hat{v}_z(\hat{z}) \simeq N_s^{1/2}$. Using typical values for electrospinning solution jets of the experimental system (PEO 3 wt% in water; see Sec. III), we may predict that the stretching occurs at $z_{\text{stretch}}/z_0 \simeq 3.5$.

A term providing the unlimited increase in an effective modulus of an almost fully stretched subchain can be introduced into Eq. (5) by replacing the linear elasticity of polymer subchains, T/ξ_0^2 , with the nonlinear $T/\{\xi_0^2[1 - (z_{n+1} - z_n)/aN_s]\}$. However, such a modification does not account well for the system behavior and the additional processes associated with high levels of polymer subchain stretching. More specifically, almost fully stretched subchains begin to disentangle, thereby raising the subchain length ξ_0 . In addition, the highly stretched polymer network begins to

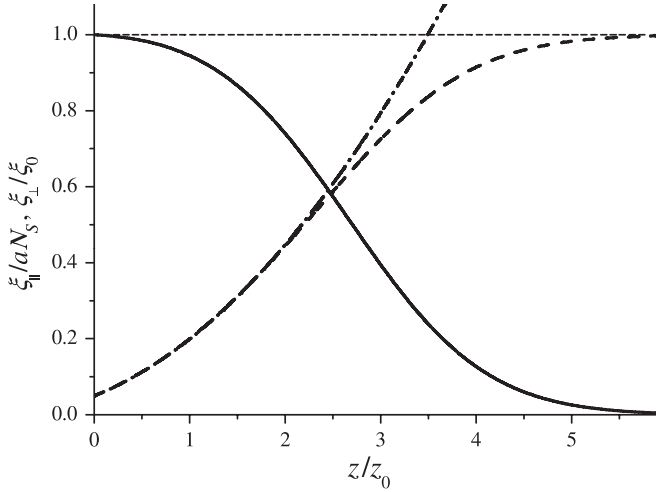


FIG. 3. Polymer network conformation. Relative radial contraction, ξ_{\perp}/ξ_0 (solid line), and relative axial stretching, ξ_{\parallel}/aN_s (dashed and dot-dashed lines), vs the relative axial position, z/z_0 . The results were obtained by the simulation (dashed and solid lines) and theoretical model (dot-dashed line). Parameters are $N_s = 400$, $\alpha = 1000$, and $\beta = 0.3$.

affect the effective viscosity of the solution, influencing the jet velocity. Furthermore, slipping of the solvent surface layer relative to the polymer network is also possible.

For these reasons we would like to restrict ourselves to the simplest model describing only the initial stage of polymer network evolution inside the electrospinning jet. Although the proposed model does not describe the final state of the polymer matrix in electrospun nanofibers, and is applicable only to the initial part of the jet where the stretching of a polymer system is not too high, it allows for analysis and understanding of the tendency in the evolution of the polymer during the electrospinning process.

Note that the transformation of subchains from a coil-like equilibrium state into a stretched state occurs as a continuous crossover, and no phase transition is observed, in contrast to the well-known coil-stretch transition, described by de Gennes [26]. Unlike stretching of an individual chain, during network stretching locally the dominant force that provides this transformation is the elastic force, whereas the hydrodynamic forces give rise to the global stretching of the network. As a result, the network subchains are subjected to the action of the network portion situated farther along the jet, a force independent of local stretching. In contrast, the force acting on an individual polymer chain under an ultrahigh velocity gradient increases with macromolecule stretching. Similar behavior, continuous crossover from a coil-like state into a stretched state was observed by Balabaev *et al.* upon examination of the state of an individual macromolecule under an external force acting on its ends [27].

D. Radial contraction

When analyzing the compression of the polymer network in a plane perpendicular to the jet, the process becomes stationary quite rapidly and can be presented as a one-dimensional (1D)

chain of springs [see Fig. 2(c)] in a steady state, described by the following differential equation:

$$\frac{T}{\xi_0^2} \{ [R_{n+1} - R_n - \xi_{\perp}] - [R_n - R_{n-1} - \xi_{\perp}] \} + a_{\text{eff}} \eta v_r(R_n) = 0, \quad (13)$$

which can be approximated by the following differential equation [using the velocity v_r from Eq. (1)]:

$$\frac{d^2 R(\rho, z)}{d\rho^2} - \kappa^2(z) R(\rho, z) = 0, \quad (14)$$

where $\rho = r/z_0$, $\kappa(z) = \kappa_0 [\xi_0/\xi_{\perp}(z)] \sqrt{1 + z/z_0}$, and $\kappa_0^2 = z_0 v_0 a_{\text{eff}} \eta / m c_{\text{net}}^2 = (v_0^2/c_{\text{net}}^2 - 1) \alpha$, ($\kappa_0 \sim 10-10^2$).

The boundary conditions for Eq. (14) are

$$\frac{dR(\rho_0)}{d\rho} - z_0 + \frac{\xi_{\perp}(z)}{z_0} \kappa^2(z) R(\rho_0) = 0, \quad R(0) = 0, \quad (15)$$

where $\rho_0 \equiv \rho_0(z) = r_J(z)/z_0$ corresponds to the jet radius in the cross section z [see Eq. (2)], and ξ_{\perp} is the lateral contraction of the mesh size due to the axial stretching ξ_{\parallel} :

$$\xi_{\perp} = \frac{3\xi_0}{2 + [1 - (a\xi_{\parallel}/\xi_0^2)^2]^{-1/2}}. \quad (16)$$

The solution of Eq. (14) with the boundary conditions (15) is

$$R(\rho, z) = \frac{z_0 \sinh[\kappa(z)\rho] / \cosh[\kappa(z)\rho_0]}{\kappa(z) \{1 + [\xi_{\perp}(z)/z_0] \kappa(z) \tanh[\kappa(z)\rho_0]\}}. \quad (17)$$

The polymer network radius, $R_P(z)$, is given at $\rho = \rho_0$ by the following form:

$$R_P(z) = \frac{z_0 \tanh[\kappa(z)\rho_0]}{\kappa(z) \{1 + [\xi_{\perp}(z)/z_0] \kappa(z) \tanh[\kappa(z)\rho_0]\}}. \quad (18)$$

For small values of argument $\kappa(z)\rho_0 \ll 1$ and $\kappa(z)\xi_{\perp}(z)/z_0 \ll 1$, Eq. (18) demonstrates no radial contraction of the polymer network, yielding

$$R_P(z) = z_0 \rho_0(z) = r_J(z). \quad (19)$$

For large values of the argument of “tanh” ($\kappa(z)\rho_0 \gg 1$) one can assume that $\tanh[\kappa(z)\rho_0] \approx 1$, so that Eq. (18) can be simplified. Taking into account the fact that $\kappa(z)\xi_{\perp}(z)/z_0 \ll 1$, in the case of finite z/z_0 one can write

$$R_P(z) = \frac{\xi_{\perp}(z)}{\xi_0} \frac{z_0}{\kappa_0 \sqrt{1 + z/z_0}}, \quad (20)$$

and in the case of large z ($z/z_0 \gg 1$) the polymer network has the following form:

$$R_P(z) = \frac{z_0^2}{\kappa_0^2 \xi_0 (1 + z/z_0)}, \quad (21)$$

indicating a constant ratio between the jet and polymer radii. However, the last asymptote lacks physical significance, as the effects dominant at this stage of the processes are not accounted for, thereby making the model inappropriate far from the jet start.

An approximation for the dependence of the polymer network radius, $R_P(z)$, on the jet radius, $r_J(z)$, can be given by

$$R_P(z) = \frac{\xi_{\perp}(z)}{\xi_0} r_J(z) \simeq \frac{3r_J(z)}{2 + \{1 - [a\hat{v}_z(\hat{z})/\xi_0]^2\}^{-1/2}}, \quad (22)$$

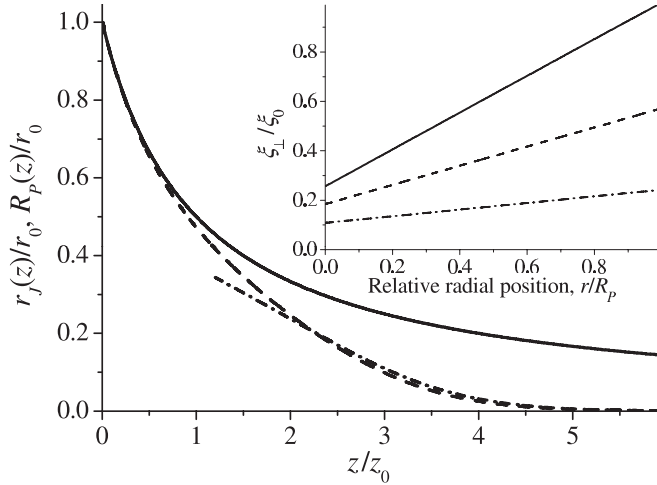


FIG. 4. Polymer network contraction. Relative jet radius r_j/r_0 (solid line) and polymer network radius R_p/r_0 : dashed line Eq. (22) and dot-dashed line Eq. (20) as a function of the axial position, z/z_0 . The inset displays radial contraction, ξ_{\perp}/ξ_0 , obtained by simulations, as a function of the relative radial position, r/R_p , at three axial positions, $z = 0$ (solid line), $z/z_0 = 2.5$ (dashed line), and $z/z_0 = 3.5$ (dot-dashed). Parameters are the same as in Fig. 3.

showing that the axial stretching is the dominant factor determining the network radius, while the radial hydrodynamic compression has a negligible effect. When presenting the relationship, $R_p(z)/r_0$, as a function of position z along the jet and comparing it to Eq. (20), a rapid narrowing of the network radius is observed with respect to the jet radius (see Fig. 4). The expected outcome is a substantial rise in polymer concentration toward the jet center.

Summarizing the above results, one can conclude that no contraction of the polymer network occurs at the initial region of the jet. The intermediate asymptote demonstrates that the radial hydrodynamic effect is negligible, and that longitudinal stretching acts as the dominant factor affecting polymer network contraction, resulting in shortened distances between adjacent topological knots in the transversal direction. In the case of very large z ($z/z_0 \gg 1$), the form of the polymer network conforms to that of the jet. Note that the last asymptote is barely discernible in a real system, due to rapid solvent evaporation in this region, which acts as the dominant factor determining the state of the polymer system.

E. Conformational state of polymer subchains in the jet (numerical simulations)

The simplest way to examine the modification of the local conformational state of individual polymer chains along the jet is by application of the 3D random-walk model under an external field, with the help of numerical simulations. An effective potential, $U(x)$, between two adjacent topological knots connected by a polymer subchain, gives rise to “convective flux” (in addition to diffusive), which results in a nonzero end-to-end distance of subchains. The gradient of this potential, $\vec{\nabla} U(x)$, is an external force, \vec{F} , constituted of hydrodynamic and elastic forces acting on each subchain. Indeed, the direction of each step is determined

by the stepping probabilities arising from the local effective potential

$$P_j^{\pm} = \frac{\exp(\pm F_j a/T)}{2 \sum_j \cosh(F_j a/T)}; \quad j = z, \rho, \varphi, \quad (23)$$

where a is the above-introduced monomer (or Kuhn segment) scale.

In the equilibrium the effective external forces in all directions are the identical, $F_j^{(0)} \equiv F_0$, and result in the mesh size, ξ_0 . Thus, the force F_0 is determined by the following equation:

$$\tanh(F_0 a/T) = 3/\sqrt{N_s} = 3a/\xi_0. \quad (24)$$

The stretching of a subchain along the jet flow direction can be accounted for by an increase in the potential gradient, $F_z = F_0 + \Delta F$. At the same time, this stretching results in transversal contraction of the polymer subchain due to redistribution of probabilities in the direction choice during the random walk. The additional potential gradient, ΔF , results in the stretching of a subchain, ξ_{\parallel} , which can be determined by the following equation:

$$\xi_{\parallel} = \frac{(\xi_0/a) \sinh[(F_0 + \Delta F)a/T]}{\cosh[(F_0 + \Delta F)a/T] + 2 \cosh(F_0 a/T)} \xi_0. \quad (25)$$

Compression in the perpendicular (radial) direction corresponding to this stretching can be expressed as

$$\frac{\xi_{\perp}}{\xi_{\parallel}} = \frac{\sinh(F_0 a/T)}{\sinh[(F_0 + \Delta F)a/T]}. \quad (26)$$

Note that Eq. (26) agrees with Eq. (16).

The potential gradient, ΔF_n , at subchain n comprises two components: a potential gradient corresponding to the elastic force, approximately equal to the potential gradient at the preceding subchain $n-1$, ΔF_{n-1} , and, an additional potential gradient, δF_n , corresponding to the hydrodynamic friction force acting on subchain n . Note that, as demonstrated above, the elastic force is the dominant factor acting on a subchain, and that it arises from the hydrodynamic interactions. Therefore, both the elastic and hydrodynamic forces acting on subchain n are determined by the jet velocity gradient.

The local velocity gradient, $\nabla v_{z,n}$, is practically constant within the scale of an individual subchain and yields an average velocity difference of magnitude $\frac{1}{2} \nabla v_{z,n} \xi_{\parallel,n}$ between the dilute fluid and the subchain ($\xi_{\parallel,n}$ is the mesh size of subchain in the flow direction). This velocity difference generates a friction force on each monomer (or Kuhn segment) of length a , with a corresponding average additional potential gradient of

$$\delta F_n = \frac{1}{2} k a \eta \xi_{\parallel,n} \nabla v_{z,n}, \quad (27)$$

where the dimensionless constant $k \propto 1$ is a geometric factor that depends on the segment's shape. Once the potential gradient, δF_n , is known for a subchain, the stepping probabilities in all six directions can be calculated from Eq. (23), and the random-walk algorithm can be applied by stepping sequentially through all the segments of the subchain.

The polymer network conformation, determined by the extension and contraction of each subchain, can be derived

by sequentially calculating the following: By knowing the state of the previous ($n - 1$) subchain, the position of the n th topological knot can be calculated as $z_n = z_{n-1} + \xi_{\parallel,n-1}$; the corresponding velocity gradient is then determined as $\nabla v_{z,n} = dv_z(z_n)/dz_n$, with the help of Eq. (1), and, assuming an extension of $\xi_{\parallel,n} \approx \xi_{\parallel,n-1}$ for the n th subchain, the additional potential gradient δF_n can be calculated from Eq. (27). The random-walk simulation with the effective force $F_n = F_0 + \sum_1^n \delta F_m$ allows one to determine the subchain extension, $\xi_{\parallel,n}$ [Eq. (25)], as well as the subchain radial contraction $\xi_{\perp,n}$ [Eq. (26)], due to redistribution of probabilities in the directions of choice during the random walks. This procedure starts at the first subchain, with the initial potential gradient F_0 [Eq. (24)] and is sequentially repeated for all subchains in the network.

The simulation uses only one dimensionless parameter $\beta = ka^2\eta v_0/T$ ($\sim 0.1-1$). Each subchain is represented by a succession of random steps of size a . The jet parameters z_0 and v_0 are obtained from experimental measurements. The effective viscosity η is a free simulation parameter, and its resulting values, lying between the viscosity of a solvent ($\sim 10^3$ Pa·s) and the viscosity of a semidilute solution (~ 1 Pa·s), are physically plausible. The mesh sizes ξ_{\parallel} and ξ_{\perp} , obtained from the simulation as a function of position along the jet, are depicted in Fig. 3. A difference between the theoretical model and the simulation is observed at high elongations, as the model does not account for the restriction on elongation due to the finite contour length of subchains.

A similar procedure is applied to the radial simulation, for several cross sections along the jet, starting with subchains at the jet perimeter, and continuing the sequential calculation toward the jet center. The radial mesh size, $\xi_{\perp}(r,z)$, obtained from the simulation as a result of the combined effect of axial stretching and radial compression, is depicted in the inset in Fig. 4. Compression due to radial hydrodynamic forces induces a further rise in polymer concentration toward the jet center, most notable at the initial region of the jet, in addition to the rise caused by axial stretching, as described before.

III. EXPERIMENTAL

A. Materials and methods

In-line fast x-ray phase-contrast imaging [28,29] was used to measure the radiation absorption of the straight region of an electrospinning jet. The experiment was carried out at the 32-ID Beamline, Advanced Photon Source (APS), Argonne National Lab, using a partially coherent undulator x-ray white beam. A scheme of the experimental setup, consisting of the x-ray imaging system and the electrospinning apparatus, is presented in Fig. 5(a).

The x-ray beam was generated from the synchrotron's electron storage ring with a dominant harmonic at 13 keV, corresponding to a wavelength of 0.95 \AA [28]. The x-ray pulses were each 472 ns long, separated by a $3.68 \mu\text{s}$ time gap. A slow shutter opened the beam path at 1 Hz, and a fast shutter enabled isolation of single pulses. After penetrating the electrospinning jet, the transmitted radiation was imaged on a fast scintillator crystal (LYSO:Ce, 40 ns decay time), which converted the x-ray radiation to visible light. The scintillator's image was

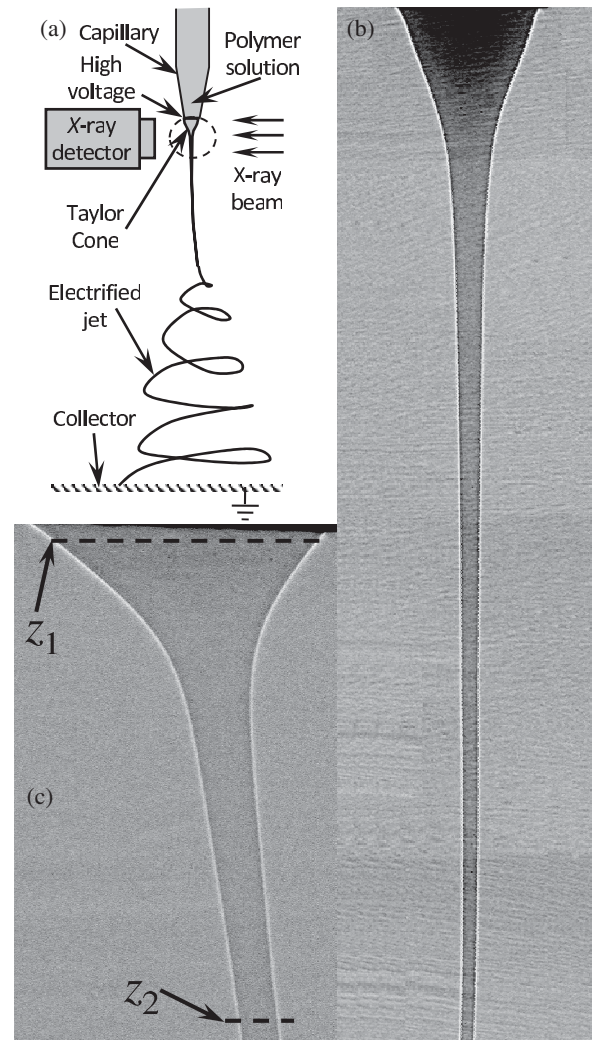


FIG. 5. (a) Schematics of electrospinning and fast in-process x-ray imaging. The imaged region is circled. (b) Rectilinear section of the jet (5 mm length), consisting of a sequence of 10 images. Electrospinning of a solution of 5 wt% PEO (Mw 600 kDa) in water; electric field 0.6 kV/cm with gap of 6.5 cm, flow rate 3.2 ml/h. (c) Zooming on the Taylor cone. The lines at $z_1 = 0.02$ mm and $z_2 = 0.5$ mm indicate the cross sections of the absorption measurements across the electrospinning jet. Electrospinning of a solution of 3 wt% PEO (Mw 600 kDa) in water; electric field 1.6 kV/cm with gap of 6.5 cm, flow rate 2 ml/h.

recorded by a $1280\text{H} \times 1024\text{V}$ CCD camera with pixel size of $6.7 \times 6.7 \mu\text{m}^2$ via a folding mirror and a $\times 10$ objective optics. The target (i.e., the scintillator) was distanced 10 cm from the jet, and the beam size on the target was large enough to cover the effective camera field-of-view of $0.857\text{H} \times 0.686\text{V} \text{ mm}^2$.

A remotely controlled motorized stage enabled x,y,z positioning of the electrospinning chamber, during a single session, so that up to 8 mm of jet length could be imaged by capturing a sequence of images along the jet [see Figs. 5(a) and 5(b)]. Images were recorded with depth of 16-bit grayscale, at a rate of 1 Hz. Dark and background images were also collected and used for removal of the background spatial nonuniformity and for setting the background intensity to 1. Jet radius measurements, necessary

for the absorption analysis, were adjusted for the edge diffraction pattern [the white corona visible in Figs. 5(b) and 5(c)].

The polymers, purchased from Sigma-Aldrich, were PEO (Mw 600 kDa) dissolved in water at 3 wt% and 5 wt%, and PMMA (Mw 70 kDa) dissolved in CHCl_3 (chloroform) at 15 wt%. The polymer solution was injected by a syringe pump into a 25-gauge capillary needle installed on top of an enclosed plastic chamber, at volumetric feed rates ranging from 0.75 to 6 ml/h. A high-voltage power supply created a potential difference ranging from 4 to 14 kV, across a gap of 6.5 cm between the needle and the collector base, creating a nominal electric field of 0.6 to 2.2 kV/cm. The experiments were conducted at room temperature at a relative humidity of 40%.

Transmission measurements were derived from pixel intensity. The intensity of each pixel was averaged vertically within a vertical slice of up to of 13 pixels and adjusted for the residual local background offset. Horizontal pixel averaging was avoided to retain important features across the jet. The intensity profiles across the jet (T_{exp}) were normalized by the intensity calculated for the polymer solution at rest (T_{sim}), using a wave propagation simulation that took into account the overall optical effects due to absorption and scattering. The simulation was based on the Fresnel equation in the paraxial approximation [30]. The most relevant experimental parameters were included in the code, such as jet geometry and energy-dependent absorption coefficients and refraction indices, as well as source size, energy spectrum, and detector point-spread function. The resulting normalized intensity profiles across the jet represent the changes in the jet x-ray absorption due to polymer concentration variations.

B. Measurements of polymer concentration variations across the jet

Profiles of the radiation transmission T_{exp} were measured across the jet close to the jet start as well as farther along the jet, for PEO as well as for PMMA. Measured profiles of T_{exp}

for PEO 3 wt%, overlaid on the simulated transmission of a stationary jet T_{sim} are plotted in Fig. 6. Close to the jet start, T_{exp} and T_{sim} almost coincide, as expected for homogeneous polymer solution [see Fig. 6(a)], whereas farther along the jet, T_{exp} rises above T_{sim} at the jet center, indicating a change in the local absorption coefficient [see Fig. 6(b)]. Since in this test case the polymer used has a lower absorption coefficient than its respective solvent, the decrease in absorption reflects a polymer concentration increase at the jet center.

It should be noted that the measured transmitted x-ray beam T_{exp} is the result of the incident beam attenuation due to both absorption and scattering of the materials contained in the jet. Because of the nonzero distance between the jet and the target, scattering effects of the collimated beam can become significant, especially for small objects [31] such as the electrospinning jet. Therefore, the radiation transmission can be written using the Beer–Lambert law in the following form:

$$T(r, z) = g(r, z) \exp[-d(r, z) \alpha(r, z)], \quad (28)$$

where $g(r, z)$ is a form factor describing the scattering effect; $d(r, z) = 2r_J(z) \sqrt{1 - [r/r_J(z)]^2}$ is the length traveled by the beam through the jet at the radial position r and $r_J(z)$ is the local jet radius at position z ; and $\alpha(r, z) = \varepsilon_P c_P(r, z) + \varepsilon_S c_S(r, z)$ is the absorption coefficient of polymer solutions, ε_P and ε_S denote the x-ray mass absorption coefficients of the polymer and solvent, respectively, and $c_P(r, z)$ and $c_S(r, z)$ denote the mass concentrations [32].

Since the wave propagation simulation also incorporates both absorption and scattering, for our purpose of detecting polymer concentration variations across the jet, we can compare the radiation transmissions obtained experimentally T_{exp} to the wave propagation simulation through the homogenous polymer solution T_{sim} . Assuming that both experiment and simulation result in the similar scattering effect ($g_{\text{exp}}(r, z)/g_{\text{sim}}(r, z) \cong 1$), normalization T_{exp} by T_{sim} reduces the influence of the scattering. Thus, the average variations in the measured absorption coefficient, $\Delta\alpha(r, z)$, with respect to the value of the fluid at rest, obtained by the wave

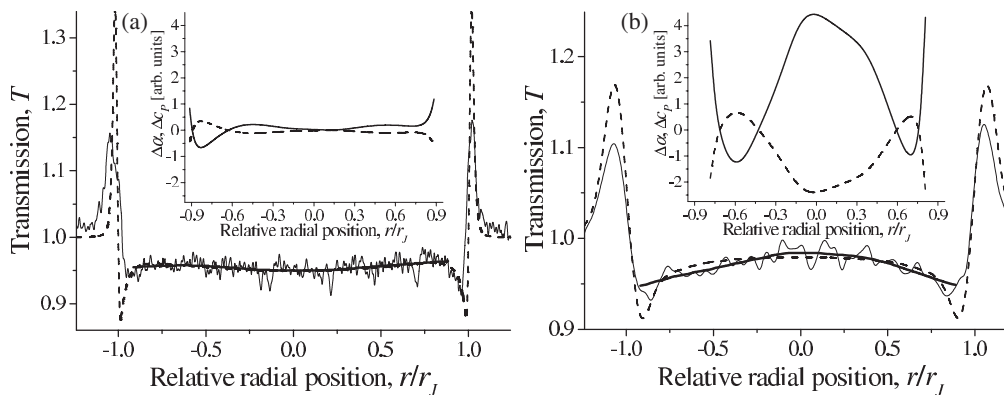


FIG. 6. Typical absorption measurements across the electrospinning jet of a solution of 3 wt% PEO (Mw 600 kDa) in water at the two z positions indicated in Fig. 5(c) (electric field 1.6 kV/cm, flow rate 2 ml/h). The measured transmission, T_{exp} , (thin solid line) and its smoothing (thick solid line) compared to simulated transmission, T_{sim} (dashed line). The inset displays calculated variations in x-ray absorption coefficient, $\Delta\alpha(r, z)$ (dashed line), and resulting variations in the local polymer mass concentration, $\Delta c_P(r, z)$ (solid line). (a) $z = 0.02$ mm, $r_J(z) = 120$ μm ; and (b) $z = 0.5$ mm, $r_J(z) = 22$ μm .

propagation simulation can be calculated with the help of the following equation:

$$\Delta\alpha(r, z) = -\frac{1}{d(r, z)} \ln \left[\frac{T_{\text{exp}}(r, z)}{T_{\text{sim}}(r, z)} \right]. \quad (29)$$

Note that although Eq. (29) cannot fully compensate for the scattering effects, the obtained $\Delta\alpha(r, z)$ is sufficient, as it represents a trend, rather than an exact value. Typical results of the change in the absorption coefficient across the jet are presented in the insets of Fig. 6. Almost no change in the absorption coefficient across the jet was observed close to the jet start, whereas a distinct change in the absorption coefficient was observed farther along the jet.

Variations in the local polymer concentration can be calculated using the obtained variations in the absorption coefficient, $\Delta\alpha(r, z)$, from Eq. (29), as

$$\Delta c_P(r, z) = \frac{\Delta\alpha(r, z)}{\varepsilon_P - \varepsilon_S(\rho_S/\rho_P)}, \quad (30)$$

where ρ_P and ρ_S are the densities of the polymer and solvent, respectively.

For the PEO test case, the x-ray mass absorption coefficients and densities are $\varepsilon_P = 1.51 \text{ cm}^2/\text{g}$ and $\rho_P = 1.13 \text{ g}/\text{cm}^3$ (PEO); and $\varepsilon_S = 2.29 \text{ cm}^2/\text{g}$ and $\rho_S = 1 \text{ g}/\text{cm}^3$ (water) [33]. Substituting these x-ray material properties, the apparent change in polymer concentration can be calculated (insets of Fig. 6). While almost no change in absorption coefficient, and hence in polymer concentration, was observed across the jet close to the jet start [see inset in Fig. 6(a)], the absorption coefficient varied across the jet with respect to its initial value, when measured at points farther along the jet, indicating a nonuniform polymer concentration distribution [see inset in Fig. 6(b)]. A distinct decrease in absorption coefficient, and matching rise in concentration, was observed close to the jet center, while the absorption coefficient increased and concentration decreased, when measured at greater distances from the center, as expected from the redistribution of the polymer across the jet. Note also the sharp decrease in absorption coefficient at the jet boundary, which occurred irrespective of the position along the jet. This phenomenon may be caused by surface interaction between the polymer solution and the x-ray radiation. Similar behavior was observed in a PMMA test, demonstrating that polymer network stretching and lateral contraction are noticeable, even in cases of rapid solvent evaporation.

These experimental results are in agreement with our theoretical analysis that predicted fast network stretching and lateral contraction at high-velocity gradients, resulting in increased polymer concentration toward the jet center. The absorption measurements demonstrated that stretching is low and insignificant close to the jet start. However, at a distance of only 0.5 mm from the jet start, a significant rise in polymer concentration is observed at the jet center, indicating that stretching is already very high at this position. The theoretical analysis predicts a high stretching at the same region (see Fig. 3).

IV. CONCLUSIONS

The dynamics of the polymer network structure within the electrospinning jet of highly entangled, semidilute polymer solutions was studied both theoretically and experimentally. The theoretical modeling demonstrated that the polymer network can transform from a free state to an almost fully stretched state under extreme longitudinal acceleration, within less than 1 millimeter from the jet start. The stretching of the network is accompanied by substantial lateral contraction that leads to a rise in polymer concentration at the jet center, as confirmed by x-ray absorption measurements of the jet. This rise in polymer concentration can account for the formation of homogeneous fiber structure, as observed in polymer systems under certain electrospinning conditions.

At first glance, the short distance required for such a dramatic change in the conformational state of a polymeric subsystem in solution is unexpected from a physical point of view. Firstly, the well-known de Gennes criterion for coil-stretch transition, $\dot{\varepsilon}\tau_{\text{relax}} > \theta_{\text{cr}} = 0.5$ [26], is not valid in the region of macromolecule stretching during electrospinning (according to the experimental data for the system in question, $\dot{\varepsilon}\tau_{\text{relax}} < \theta_{\text{cr}}$). This discrepancy can be explained when considering the fact that the system presented here involves an entangled polymer network. In this case, the dominant local force, inducing macromolecule stretching, is the elastic force arising from the action of the portion of the polymer network situated farther along the jet, whereas the hydrodynamic forces give rise to the global network stretching. Conversely, the de Gennes criterion corresponds to an individual polymer macromolecule and is therefore not suitable for the estimation of the conformational state of the polymeric subsystem of the spinning jet.

In addition, the experimental observations demonstrate that further jet acceleration, but no further polymer chain elongation, is possible. The reasonable question is: What happens with the polymer subsystem of the jet during the further stage of the spinning. To date, no experimental data are available with regard to the internal evolution of the electrospinning jet at later stages of spinning, and this question remains an open problem. We surmise that disentanglement and topological reordering of the polymer network will be observed; these processes call for thorough examination.

Nevertheless, the obtained results allow predicting the stretched nonequilibrium conformational state of a polymer matrix inside electrospun nanofibers, although partial relaxation of this ordered microstructure can still occur after formation. Thus, the final state of the internal microstructure of electrospun nanofibers remains nonequilibrium, affecting their mechanical and thermodynamic properties. Note, however, that these unique properties cannot be explained only by nano-object microstructure or by processing effects. In our opinion, the formed microstructure sets a new internal scale within the nanofiber, and the unique properties of polymer nanofibers can be related to confinement of such microstructure [1].

ACKNOWLEDGMENTS

We gratefully acknowledge the financial support of the United States-Israel Binational Science Foundation (Grant

No. 2006061) and the RBNI-Russell Berrie Nanotechnology Institute. Use of the Advanced Photon Source, an Office of Science User Facility operated for the US Department of Energy (DOE) Office of Science by

Argonne National Laboratory, was supported by the US DOE under Contract No. DE-AC02-06CH11357. AA acknowledges support from the Kamea Program, Israel Ministry of Absorption.

-
- [1] A. Arinstein, M. Burman, O. Gendelman, and E. Zussman, *Nat. Nanotechnol.* **2**, 59 (2007).
- [2] Y. Ji *et al.*, *Europhys. Lett.* **84**, 56002 (2008).
- [3] S. Cuenot, C. Fréty, S. Demoustier-Champagne, and B. Nysten, *Phys. Rev. B* **69**, 165410 (2004).
- [4] H. Schonherr and C. W. Frank, *Macromolecules* **36**, 1188 (2003).
- [5] S. Cuenot, S. Demoustier-Champagne, and B. Nysten, *Phys. Rev. Lett.* **85**, 1690 (2000).
- [6] G. B. McKenna, *Eur. Phys. J. Spec. Topics* **141**, 291 (2007).
- [7] H. R. Brown and T. P. Russell, *Macromolecules* **29**, 798 (1996).
- [8] P. G. de Gennes, *Eur. Phys. J. E* **2**, 201 (2000).
- [9] M. Burman, A. Arinstein, and E. Zussman, *Europhys. Lett.* **96**, 16006 (2011).
- [10] D. H. Reneker, A. L. Yarin, H. Fong, and S. Koombhongse, *J. Appl. Phys.* **87**, 4531 (2000).
- [11] M. M. Hohman, M. Shin, G. Rutledge, and M. P. Brenner, *Phys. Fluids* **13**, 2201 (2001).
- [12] Y. M. Shin, M. M. Hohman, M. P. Brenner, and G. C. Rutledge, *Polymer* **42**, 09955 (2001).
- [13] P. Gupta, C. Elkins, T. E. Long, and G. L. Wilkes, *Polymer* **46**, 4799 (2005).
- [14] D. H. Reneker, A. L. Yarin, E. Zussman, and H. Xu, *Adv. Appl. Mech.* **41**, 43 (2007).
- [15] L. M. Bellan, H. G. Craighead, and J. P. Hinestroza, *J. Appl. Phys.* **102**, 094308 (2007).
- [16] T. Han, A. L. Yarin, and D. H. Reneker, *Polymer* **49**, 1651 (2008).
- [17] L. Larrondo and R. S. J. Manley, *J. Polym. Sci. Polym. Phys.* **19**, 921 (1981).
- [18] J. S. Stephens, S. Frisk, S. Megelski, J. F. Rabolt, and D. B. Chase, *Appl. Spectrosc.* **55**, 1287 (2001).
- [19] P. Dayal, J. Liu, S. Kumar, and T. Kyu, *Macromolecules* **40**, 7689 (2007).
- [20] C. L. Casper, J. S. Stephens, N. G. Tassi, D. B. Chase, and J. F. Rabolt, *Macromolecules* **37**, 573 (2004).
- [21] A. J. Guenther, S. Khombhongse, W. Liu, P. Dayal, D. H. Reneker, and T. Kyu, *Macromol. Theor. Simul.* **15**, 87 (2006).
- [22] P. Dayal and T. Kyu, *Phys. Fluids* **19**, 107106 (2007).
- [23] S. Koombhongse, W. X. Liu, and D. H. Reneker, *J. Polym. Sci. Polym. Phys.* **39**, 2598 (2001).
- [24] A. Arinstein and E. Zussman, *J. Polym. Sci. Polym. Phys.* **49**, 691 (2011).
- [25] S. N. Reznik and E. Zussman, *Phys. Rev. E* **81**, 026313 (2010).
- [26] P. G. de Gennes, *J. Chem. Phys.* **60**, 5030 (1974).
- [27] N. K. Balabaev, I. P. Borodin, T. I. Borodina, and T. N. Khazanovich, *Polym. Sci. A* **52**, 655 (2010).
- [28] Y. Wang, X. Liu, K.-S. Im, W.-K. Lee, J. Wang, K. Fezzaa, D. L. S. Hung, and J. R. Winkelman, *Nat. Phys.* **4**, 305 (2008).
- [29] K. S. Im, K. Fezzaa, Y. J. Wang, X. Liu, J. Wang, and M. C. Lai, *Appl. Phys. Lett.* **90**, 091919 (2007).
- [30] R. V. Reeves, J. D. E. White, E. M. Dufresne, K. Fezzaa, S. F. Son, A. Varma, and A. S. Mukasyan, *Phys. Rev. B* **80**, 224103 (2009).
- [31] A. Sasov, in *Proceedings of the 9th European NDT Conference* (Berlin, Germany, 2006).
- [32] R. J. Roe, *Methods of X-ray and Neutron Scattering in Polymer Science* (Oxford University Press, New York, 2000).
- [33] E. Gullikson, http://henke.lbl.gov/optical_constants/.